



# Leveraging topological data analysis to estimate bone strength from micro-CT as a surrogate for advanced imaging

John Rick Manzanares<sup>1,2</sup> , Richard Leslie Abel<sup>3</sup> , and Paweł Dłotko<sup>1</sup> 

<sup>1</sup>Dioscuri Centre in Topological Data Analysis, Institute of Mathematics of the Polish Academy of Sciences, 00-656 Warsaw, Poland, <sup>2</sup>International Environmental Doctoral School, University of Silesia in Katowice, 41-200 Sosnowiec, Poland, <sup>3</sup>Department of Surgery and Cancer, Faculty of Medicine, Imperial College London, United Kingdom

## Abstract

Accurate bone strength prediction is essential for assessing fracture risk, particularly in aging populations and individuals with osteoporosis. Bone imaging has evolved from X-rays and DXA to clinical computed tomography (CT), and now to advanced modalities such as high-resolution peripheral quantitative CT and synchrotron radiation CT, which offer unprecedented resolution of bone microarchitecture. However, analytical methods have not kept pace with these imaging advances. This study applied topological data analysis (TDA) to extract biomechanically relevant features from high-resolution bone images, offering a new framework for bone strength prediction. We extracted topological features, specifically those derived from persistent homology, and combined them with standard bone morphometric descriptors to train machine learning models for apparent strength prediction. Models based solely on topological features outperformed those using traditional morphometrics, highlighting TDA's ability to capture biomechanically relevant structure. In particular, internal voids, often dismissed as imaging noise, proved to be the most predictive. While limited by dataset size and class imbalance, these results suggest that TDA offers a promising approach for advancing osteoporosis risk assessment.

## Plain Language Summary

Bone compressive strength may serve as a direct proxy for bone fragility. However, analytical methods have not kept pace with advances in imaging technologies. In this study, we investigated the potential of topological features derived from bone images to capture structural characteristics that predict mechanical strength. Our findings suggest that topological information may serve as a biomarker for bone fragility and related diseases, despite limitations in dataset size and balance.

**Keywords** Persistence Image, Cubical Homology, Signed Distance Transform

## 1. INTRODUCTION

Over the past decades, bone imaging has evolved from conventional X-rays and dual-energy X-ray absorptiometry to clinical computed tomography (CT) and other advanced modalities. Among these, high-resolution peripheral quantitative CT (Gazzotti et al., 2023) provides detailed assessment of bone micro-architecture, with the second-generation scanner (XtremeCT II), offering improved resolution, shorter scan times, and direct measurement of trabecular and cortical parameters. For higher-resolution, synchrotron radiation (SR) micro-CT (Larrue et al., 2011) offers significant advantages over standard micro-CT, providing high-resolution three-dimensional (3D) imaging with excellent signal-to-noise ratio. SR micro-CT has been used to study trabecular micro-architecture and the propagation of micro-cracks under mechanical loading, although early studies on trabecular bone used relatively low resolution for micro-damage assessment.

## PREPRINT

Submitted Dec 03, 2025

### Correspondence to

John Rick Manzanares  
jdolormanzanares@impan.pl

### Funding

This project has received funding from the European Union Horizon Europe research and innovation programme under the Marie Skłodowska-Curie Actions (MSCA) grant agreement No. 101120290 (GAP).

### Competing Interests

The authors declare no competing interests.

Although imaging technologies have advanced rapidly, the analytical methods used in clinical practice have remained largely unchanged. Current gold-standard measurements, such as global bone mineral density, have notable limitations, including high cost and susceptibility to measurement errors (Morgan & Prater, 2017). Moreover, while low-resolution imaging can capture some trabecular features comparably to high-resolution methods, it fails to resolve finer details such as trabecular thickness (Issever *et al.*, 2009). Standard morphometric descriptors summarize bone structure through global parameters that overlook fine-scale architectural nuances (Fanuscu & Chang, 2004). As a result, much of the information in high-resolution scans, such as the topological organization, remains underutilized.

To address this analytical gap, this study applied topological data analysis (TDA), specifically persistent homology, to standard micro-CT images as a proxy for higher-resolution imaging. This approach introduces a novel framework for quantifying biomechanically relevant structural features that may be more predictive of bone strength than conventional metrics. Topological methods emphasize the structural and relational properties of bone, and persistent homology has already shown promise in capturing microstructural patterns from nonlinear microscopy images (Pritchard *et al.*, 2023). By identifying and quantifying multi-scale features, including connected components and loops, within trabecular microarchitecture, this study explores how topological descriptors can complement standard diagnostics and offer a computational analogue to bone biopsy.

## 2. BONE MORPHOMETRY

Bone morphometry involves the use of computational and statistical methods to extract quantitative and meaningful insights from bone specimen images. This section provides an overview of the utilized image dataset, detail the image segmentation process, and define the key morphometric characteristics commonly extracted and analyzed.

### 2.1. Trabecular Bone Specimens and Imaging Protocol

Trabecular bone is a complex, porous structure whose microarchitecture is critical to skeletal mechanical competence. Standard micro-CT of specimens is used to provide the ground-truth data required to develop and validate novel analytical methods aimed at closing this translational gap.

Trabecular bone specimens were imaged using standard micro-CT to generate 3D reconstructions. Following imaging, compression tests were performed to measure the force required to induce failure, providing the apparent bone strength (in MPa) against which all derived architectural metrics were compared.

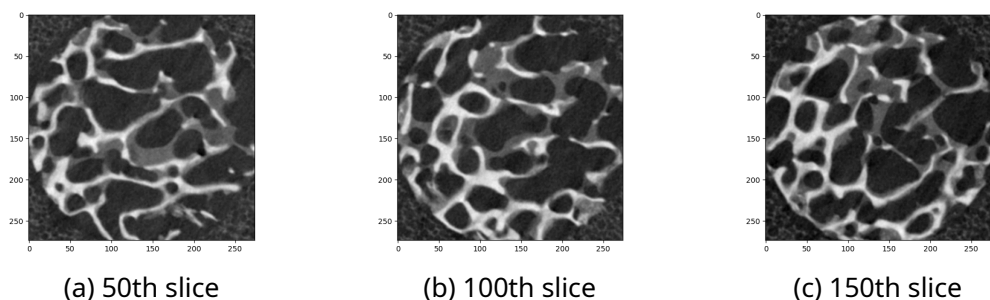


Figure 1: Axial slices from the 3D micro-CT image of a trabecular bone specimen.

The dataset is comprised of 24 micro-CT scans: 19 from the fractured (FX) group, consisting of fracture donors with a history of alendronate therapy; 3 from the non-fracture (NF) group, consisting of elderly donors with no history of bone metabolic disease, fracture or bone metabolic therapy; and 2 from the osteoarthritis (OA) group, consisting of osteoarthritis donors who underwent hip-replacement surgery. More information about the method of obtaining the dataset is available in (Jin, 2016).

Each 3D scan consisted of 416 to 534 axial slices, with spatial resolutions ranging from  $267 \times 267$  to  $346 \times 346$  pixels. Voxel spacing was isotropic (20-25 micrometers), and all images were stored as 16-bit grayscale. Representative axial slices are shown in Figure 1.

## 2.2. Image Segmentation

The analysis of bone microarchitecture requires converting the acquired 3D grayscale images into binary representations that explicitly delineate the bone phase from the void phase.

A micro-CT image is mathematically represented as a function  $I : D \subset \mathbb{Z}^3 \rightarrow \mathbb{Z}$ , where  $D$  is the discrete domain, and  $I(x)$  is the intensity at voxel  $x \in D$ . The segmentation process, known as *binarization*, transforms this grayscale image  $I$  into a binary image  $B : D \rightarrow \{0, 1\}$ , where voxels mapped to 1 denote the bone phase (foreground) and those mapped to 0 denote the void phase (background). This transformation is typically achieved via *thresholding*:

$$B(x) = \begin{cases} 0 & \text{if } I(x) \leq T(x) \\ 1 & \text{if } I(x) > T(x) \end{cases}$$

where  $T(x)$  is the threshold applied at voxel  $x$ . For trabecular bone, non-uniform intensity and noise necessitate the use of *local thresholding*, where  $T(x)$  is determined by local statistics within a closed neighborhood

$$N(x) = \{y \in D \mid d_\infty(x, y) \leq r\}$$

where  $d_\infty(x, y) = \max_i \{|x_i - y_i|\}$  is the Chebyshev distance. For a chosen  $r \in \mathbb{Z}$ , the neighborhood of  $x \in D$  is a cubic window centered at  $x$ , consisting of all points  $D$  that are two cubes (horizontal, vertical, or diagonal) away. The expression  $2r + 1$  corresponds to the *window size*.

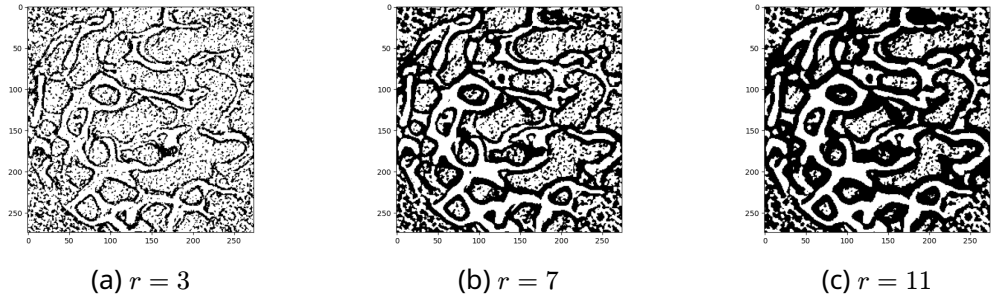


Figure 2: The slice in Figure 1b binarized with various window sizes  $r$ .

To assess the sensitivity of subsequent morphometric analysis (and ultimately TDA) to the segmentation method, three distinct local thresholding techniques were implemented and compared. A study (Engelkes, 2021) on segmentation of synthetic micro-CT volumes recommends using a local thresholding with the (1D) Otsu method. The standard Otsu method applies independently to the intensity histogram of each local neighborhood to determine  $T(x)$ . This method is computationally efficient and relies solely on local intensity contrast.

Next, a modified approach based on (Park *et al.*, 2023) enforced an additional contrast constraint  $\delta$  to the local Otsu decision. In this approach, a voxel  $x$  is classified as bone only if  $I(x) > T(x)$  and the relative difference between the class means (bone and void) within the neighborhood exceeds a user-defined  $\delta$ . This reduces misclassification in low-contrast regions. A Python implementation of this method is available at <https://github.com/jhnrckmznrs/modifiedOtsu>.

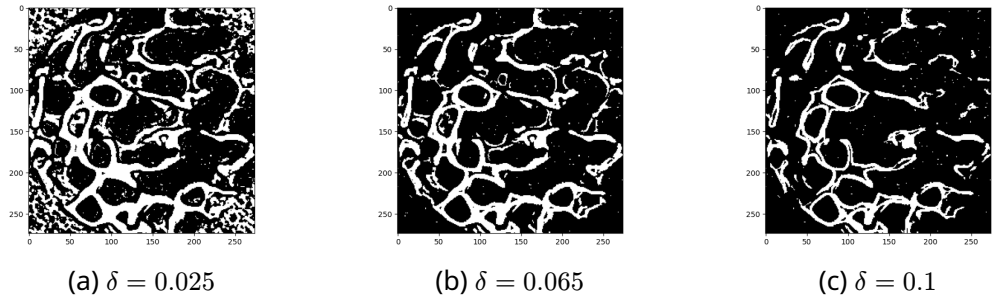


Figure 3: The slice in Figure 1b binarized with a window size of 7 and various  $\delta$  values.

Lastly, the 2D Otsu thresholding (Zhang & Hu, 2008) incorporates spatial context by determining the optimal threshold pair  $(t_g, t_m)$  on a joint 2D histogram of voxel intensity  $I(x)$  and local mean intensity  $m(x)$  across the entire image. This maximization of between-class variance in the 2D domain typically yields a more stable segmentation by accounting for neighborhood characteristics. A Python implementation of the extended method is available at <https://github.com/jhnrckmznrs/otsu2D>.

Figure 2, Figure 3, and Figure 4 illustrate the impact of the window size  $r$ , the contrast parameter  $\delta$ , and the intensity-mean window size pairs on the resulting binary images for these methods.

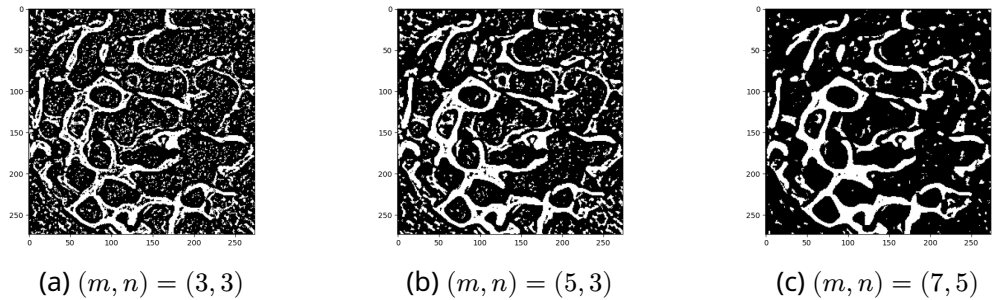


Figure 4: The slice in Figure 1b binarized using 2D Otsu with various intensity-mean window size pairs  $(m, n)$ .

### 2.3. ImageJ Software

In bone imaging, standard features commonly derived from these images known as *morphometric parameters* inform on bone quality, strength, and overall skeletal health.

The open-source platform ImageJ is a powerful tool for image processing and analysis in the life sciences (Schroeder *et al.*, 2021). For skeletal research, the BoneJ plugin (Domander *et al.*, 2021) extends ImageJ's functionality to specifically quantify 3D bone micro-architecture. BoneJ calculates a variety of standard morphometric metrics from micro-CT scans, categorizing them by measures of geometry, volume, topology, and orientation.

In this study, we computed some primary descriptors available in BoneJ. These included the mean, standard deviation, and maximum values for both trabecular thickness and trabecular spacing, which captured the overall size and separation of the bone struts. We also calculated bone volume, total volume, and the resulting bone volume fraction, which quantified the amount of bone tissue present. To summarize the structure and redundancy of the trabecular network, we included the Euler number, corrected Euler number, connectivity, and connectivity density. Finally, we measured the degree of anisotropy, which quantified the directional bias of the bone structure.

Several Python-based implementations are available for computing these parameters. A faster implementation for estimating trabecular thickness and spacing was proposed (Dahl & Dahl, 2023). Volume-related parameters can be efficiently calculated using NumPy, while functions from scikit-image (Walt *et al.*, 2014) facilitate the computation of topology and connectivity measures. The degree of anisotropy was determined using

BoneJ Headless (U.S. Food and Drug Administration, 2024), a Python wrapper designed for automated BoneJ workflows. However, BoneJ Headless was not used for the previous parameters due to observed differences in execution time and performance compared to the original BoneJ plugin.

### 3. TOPOLOGICAL DATA ANALYSIS

Topological Data Analysis (TDA) leverages concepts from algebraic topology to study the shape of data through topological invariants. It provides a powerful framework for extracting and quantifying geometric features in high-dimensional datasets, including 3D medical images, by capturing structures that persist across multiple scales.

#### 3.1. Cubical Homology

Cubical complexes provide a natural framework for representing volumetric data, such as the micro-CT images. In the following statements, we introduce the necessary concepts to define and understand cubical complexes.

Let  $\mathbb{R}^d$  denote the  $d$ -dimensional Euclidean space. An *elementary interval* is either a unit interval  $[a, a + 1]$  or a degenerate interval  $[a, a] = \{a\}$ , with  $a \in \mathbb{Z}$ . An *elementary cube* in  $\mathbb{R}^d$  is a Cartesian product

$$Q = I_1 \times I_2 \times \cdots \times I_d$$

of elementary intervals  $I_j$ . The *dimension* of  $Q$  is the number of non-degenerate intervals in the product.

A *face* of a cube  $Q = I_1 \times \cdots \times I_d$  is any cube  $F = J_1 \times \cdots \times J_d$  with  $J_j \subseteq I_j$  and  $J_j$ . In this context, we write  $F \subset Q$  to mean that  $F$  is a face of  $Q$ .

**Definition 3.1.1:** A *cubical complex*  $K \subset \mathbb{R}^d$  is a finite collection of elementary cubes such that:

1. If  $Q \in K$  and  $F \subset Q$ , then  $F \in K$ .
2. If  $Q_1, Q_2 \in K$ , then  $Q_1 \cap Q_2$  is empty or some face  $F \subset Q_1, Q_2$ .

This construction aligns naturally with the micro-CT images. Each voxel can be interpreted as 3D elementary cube, and the adjacency between voxels corresponds to shared lower-dimensional elementary cubes like vertices, edges, or faces.

Let  $\mathbb{Z}_2$  be the field of two coefficients. Suppose  $E_k(K)$  is the collection of all  $k$ -dimensional cubes of a cubical complex  $K$ . For each integer  $k \geq 0$ , the *kth chain group*

$$C_k(K) = \left\{ \sum_i a_i Q_i \mid a_i \in \mathbb{Z}_2 \text{ and } Q_i \in E_k(K) \right\}$$

is the vector space over  $\mathbb{Z}_2$  spanned by all  $k$ -dimensional cubes in  $K$ . The elements of  $C_k(K)$  are called *k-chains*.

To relate chain groups of different dimensions, we construct a linear map between chain groups that differ by one in dimension. The *boundary operator*

$$\partial_k : C_k(K) \rightarrow C_{k-1}(K)$$

is the linear map that sends each  $k$ -cube to the formal sum of its  $(k - 1)$ -dimensional faces.

Using the boundary operator, we can define important subspaces of the chain groups. The *k-cycles* are elements of the subspace

$$Z_k(K) = \ker(\partial_k) \subset C_k(K),$$

consisting of all  $k$ -chains whose boundary is zero. Meanwhile, the *k-boundaries* are elements of the subspace

$$B_k(K) = \text{Im}(\partial_{k+1}) \subset C_k(K),$$

consisting of all  $k$ -chains that are the boundary of some  $(k + 1)$ -chain.

**Theorem 3.1.2:** For all  $k \geq 1$ , the boundary operators satisfy  $\partial_{k-1} \circ \partial_k = 0$ .

**Theorem 3.1.2** (Kaczynski et al., 2004) implies the important inclusion  $B_k(K) \subset Z_k(K)$  since every boundary is automatically a cycle. This inclusion is the foundation for defining homology groups.

**Definition 3.1.3:** Let  $K$  be a cubical complex. The  $k$ th homology group  $H_k(K)$  of  $K$  is the quotient group  $Z_k(K)/B_k(K)$ .

A homology group contains all  $k$ -cycles modulo  $k$ -boundaries, capturing  $k$ -dimensional topological features that are not themselves boundaries of  $(k + 1)$ -chains.

For 3D cubical complexes, the first three homology groups are nontrivial and have intuitive geometric interpretations. The 0th homology group  $H_0(K)$  corresponds to the connected components of  $K$ . The 1st homology group  $H_1(K)$  represents loops or tunnels, such as the hole inside a drinking straw. The 2nd homology group  $H_2(K)$  captures voids or cavities, like the hollow space inside a ball.

The  $k$ th Betti number  $\beta_k$  is the dimension  $\dim H_k(K)$  of the  $k$ th homology group. This number quantifies the number of independent  $k$ -dimensional topological features of  $K$ . In the case of a finite complex  $K$ , the Betti numbers are necessarily finite. This is particularly relevant for medical imaging applications, where  $K$  arises from a finite set of voxels and thus consists of only finitely many cubes.

The topological descriptors computed using the BoneJ plug-in coincides with some of the topological features in homology groups. For instance, the first Betti number  $\beta_1$  coincides with the connectivity parameter of a binary image mentioned earlier in [Section 2.3](#). Furthermore, the global topological invariant *Euler characteristic* is the alternating sum

$$\chi = \sum_{i=0}^2 (-1)^i \beta_i.$$

of the Betti numbers.

### 3.2. Persistent Homology

Viewing a micro-CT image  $I$  or any transformation  $T$  of it as a cubical complex  $K$ , we can define a function  $f : K \rightarrow \mathbb{R}$  that stores some information about the cubes. For example, in a micro-CT image, we can map

$$f(Q) = I(x)$$

a 3-dimensional cube  $Q \in K$  corresponding to a voxel  $x$  to the grayscale intensity of that voxel. For a lower-dimensional face  $Q \in K$ , we define

$$f(Q) = \min\{f(C) \mid Q \subset C \text{ and } C \in E_3(K)\}.$$

In other words, the value of a lower-dimensional face under  $f$  is the minimum intensity among all 3D cubes of which it is a face. This assignment ensures *monotonicity*: if  $Q \subset C$ , then  $f(Q) \leq f(C)$ . We can also replace  $I$  with any image transformation  $T$ .

Through the function  $f$ , we can consider regions of  $I$  (or  $T$ ) where the intensity (or value) is at most a chosen threshold. Formally, the *sublevel set* of  $f$  at a real number  $t$  is the subcomplex of  $K$  given by

$$K_{\leq t} = \{Q \in K \mid f(Q) \leq t\}.$$

**Definition 3.2.1:** A *filtration* of a cubical complex  $K$  is a nested family  $\{K_t\}_{t \in \mathbb{R}}$  of subcomplexes satisfying  $K_{t_1} \subset K_{t_2}$  whenever  $t_1 < t_2$ .

For the sublevel sets of  $K$ , the associated filtration is known as the *sublevel set filtration*.

In the perspective of a micro-CT image, the sublevel set of  $f$  at a threshold  $t_0$  consists of voxels that have intensity at most  $t_0$ . When we move across the filtration to a threshold  $t_1 > t_0$ , we add voxels with intensities in the range  $(t_0, t_1]$ . In this case, the connectivity and shape of the bone structure may change. In other words, the homology of a cubical complex changes as we move through the filtration.

Since the sublevel sets are nested, there is a natural inclusion

$$i : K_{\leq t_0} \rightarrow K_{\leq t_1}$$

that sends each cube in  $K_{\leq t_0}$  to itself in  $K_{\leq t_1}$ . This inclusion induces a linear map on the homology groups

$$i_* : H_k(K_{\leq t_0}) \rightarrow H_k(K_{\leq t_1}).$$

This inclusion summarizes how  $k$ -dimensional topological features evolve from threshold  $t_0$  to  $t_1$ . A nontrivial class in  $H_k(K_{\leq t_0})$  may still exist in  $K_{\leq t_1}$  or may become trivial as new cubes are added. Furthermore, new classes may appear in  $H_k(K_{\leq t_1})$  that were not present in  $H_k(K_{\leq t_0})$ . This is the key idea behind persistent homology.

Persistent homology records the appearance of homological features and tracks throughout the filtration in order to record their disappearance.

**Definition 3.2.2:** Let  $\{K_t\}$  be a filtration of a cubical complex  $K$ . A homology class  $[\alpha] \in H_k(K_{\leq t_b})$  is *born* at threshold  $t_b$  if it does not lie in the image of the map  $H_k(K_{\leq t'}) \rightarrow H_k(K_{\leq t_b})$  for any  $t' < t_b$ . The class  $[\alpha]$  *dies* at threshold  $t_d$  if it maps to zero under the induced map

$$H_k(K_{\leq t_b}) \rightarrow H_k(K_{\leq t_d}).$$

The multiset of all such birth–death pairs  $(t_b, t_d)$  forms the *persistence diagram*  $\text{PD}_k(K)$  of the filtration of  $K$ .

An important property of persistence diagrams is *stability* (Cohen-Steiner et al., 2006), which ensures that small perturbations in the input data lead to only small changes in the persistence diagram. This robustness is crucial for applications in medical imaging, where noise and artifacts are common.

### 3.3. Signed Distance Persistent Homology

Persistent homology applied to the micro-CT images only gives nonnegative birth and death values since intensity of voxels are always nonnegative. However, some transformations of digital images may be beneficial to understand other properties of the structure. For instance, the signed distance transform has been proven useful in medical image and topological data analysis (Song et al., 2025). This transformation encodes richer geometric and spatial information, particularly distinguishing interior from exterior topological structures. In this study, we used the Euclidean signed distance transformation.

**Definition 3.3.1:** Given a binary image  $B : \mathbb{Z}^3 \rightarrow \{0, 1\}$ , the *Euclidean signed distance transform*  $D : \mathbb{Z}^3 \rightarrow \mathbb{R}$  with isotropic spacing  $w$  is defined by

$$D(x) = \begin{cases} w \cdot \min_{y \in \partial B} d(x, y) & \text{if } B(x) = 1 \\ -w \cdot \min_{y \in \partial B} d(x, y) & \text{if } B(x) = 0 \end{cases}$$

where  $\partial B$  denotes the boundary of the foreground region and  $d(x, y)$  is the Euclidean distance.

Note that the choice of the distance may be some non-Euclidean metric. However, since the voxels are isotropic, the Euclidean distance works well and simplifies the computation.

Similar to the grayscale micro-CT images, we can consider the sublevel set filtration of the signed distance transformation of the binarized micro-CT images and compute the persistence diagrams.

Applying persistent homology to signed distance-transformed images can be interpreted in terms of both the Cartesian-plane quadrant in which points appear and the dimension of the corresponding persistence diagram. In [Definition 3.3.1](#), we inverted the usual sign placement where distances inside the structure are negative. This reversal alters the standard interpretation of persistence features and must be carefully considered when mapping diagram points to physical structures in the image.

Under this negative-void convention, the interpretation of persistence features becomes more intuitive when analyzed by dimension. For 0-dimensional features, points appearing in the second quadrant correspond to thickness variations within void spaces, capturing the spacing and size of empty regions between bone structures. In contrast, points in the first quadrant reflect the number and size of separate void components, effectively counting voids rather than bone structures.

For 1-dimensional features, those in the second quadrant detect protrusions of bone into voids or indentations in the void space akin to dimples, whereas first quadrant points enumerate loops formed by voids, corresponding to tunnels within the bone network. Points in the first quadrant highlight non-convex void regions surrounding bone surfaces, analogous to non-convex loops around structural features.

Finally, 2-dimensional features also follow a quadrant-dependent interpretation. Points in the second quadrant indicate small bone inclusions within otherwise empty regions, effectively inverting the typical interpretation of trapped voids inside bone. Meanwhile, points in the first quadrant capture the characteristic sizes of interspaces, providing a direct measure of void spacing that aligns naturally with the convention.

From a biomechanical perspective, the 0- and 2-dimensional features are especially informative because they capture complementary aspects of bone deterioration. The 0-dimensional features quantify the loss of trabecular connectivity associated with thinning or resorption, whereas the 2-dimensional features characterize the expansion of void spaces that accompany structural weakening.

#### 3.4. Stable Vector Representation

Persistence diagrams are stable but not directly compatible with standard machine learning models because they are not naturally represented as vectors. To use persistence diagrams in machine learning, they need to be transformed into finite-dimensional vector representations. A widely used approach for this purpose is *persistence images* ([Adams et al., 2017](#)).

A persistence image can be viewed as a 2D image (or function)  $f : G \subset \mathbb{Z}^2 \rightarrow \mathbb{R}$  defined on the grid  $G$  such that  $f(z)$  are determined using the persistence diagram  $\text{PD}_k(K)$  of

a cubical complex  $K$ . To measure the “influence” of each point in  $\text{PD}_k(K)$  on each pixel in  $G$ , we consider the Gaussian kernel with mean  $u$  and variance  $\sigma^2$  given by

$$\varphi_u(x, y) = \frac{1}{2\pi\sigma^2} \exp\left(-\frac{(x - b_i)^2 + (y - p_i)^2}{2\sigma^2}\right).$$

To make the measure of influence more meaningful, we transform the  $\text{PD}_k(K)$  into the *birth-lifetime* diagram

$$T_k(K) = \{(b_i, d_i - b_i) \mid (b_i, d_i) \in \text{PD}_k(K)\}.$$

Hence, we consider the Gaussian kernel  $\varphi_u$  centered at  $u = (b_i, l_i)$  for each point  $(b_i, l_i) \in T_k(K)$ . The transformation guarantees that features with longer lifetime get more influence.

For each kernel, we can also assign a weight through a function  $w : T_k(K) \rightarrow \mathbb{R}_{\geq 0}$  defined on the birth-lifetime diagram. This weight function alongside the birth-lifetime diagram and the Gaussian kernel form the persistence image.

**Definition 3.4.1:** Let  $D$  be a persistence diagram and  $G \subset \mathbb{Z}^2$  a grid. The *k-dimensional persistence image*  $f : G \rightarrow \mathbb{R}$  is defined by

$$f(z) = \sum_{u \in T_k(K)} w(u) \varphi_u(z).$$

Similar to persistence diagrams, persistence images are stable under small perturbations. Stability and vector representation make persistence images suitable as input features for machine learning models. For the weight function, we used the constant function that maps all  $u \in T_k(K)$  to 1. In the next section, the effects on the model performance as the grid resolution and the variance in the Gaussian kernel are varied.

## 4. SUPERVISED LEARNING

Supervised learning is a core paradigm in machine learning, where models are trained on labeled datasets to learn mappings from input features to target outputs. In this section, we discuss the models used for the supervised regression task, including their training and evaluation. We also assess model performance using bone morphometry and persistence homology features as input representations.

### 4.1. Machine Learning Models

The features obtained (using bone morphometry or persistent homology) from the micro-CT images and the apparent strength can be represented as pairs forming the image dataset

$$\{(x, y) \mid x \in \mathbb{R}^d \text{ and } y \in \mathbb{R}\}.$$

Regression models use the features  $x$  to predict the target variable  $y$ . Specifically, regression involves finding a function  $g : \mathbb{R}^d \rightarrow \mathbb{R}$  that approximates the underlying trend of the dataset.

There is a wide range of algorithms to find such regression function. In this study, we employed three sets of machine learning models to predict bone apparent strength from image-derived features. The selected models include *Support Vector Regression* (SVR) (Smola & Schölkopf, 2004), *Random Forest Regression* (RF) (Breiman, 2001), and *Gradient Boosted Trees* (GBT) (Friedman, 2001). These models were chosen for their complementary strengths: SVR is well-suited for handling complex nonlinear relationships, RF provides robustness against noisy or redundant features, and GBT offers strong predictive performance by sequentially refining weak learners.

All features were standardized prior to training to ensure comparability across models. The dataset was stratified by group and split into train-validation folds, with the process

repeated to obtain four distinct splits. To ensure fairness, each model was trained and validated on the same data partitions.

Hyperparameter tuning was carried out using grid search with cross-validation. For SVR, the following parameters were explored: the type of kernel (radial basis function or linear), the regularization strength (0.1, 1, 10, 100), the margin of tolerance (0.01, 0.1, 0.3), and the kernel coefficient. For RF, the number of trees (50, 100, 200), the maximum depth of each tree (10, 20, 30,  $\infty$ ), the minimum number of samples required to split a node (2, 5, 10), and the minimum number of samples per leaf (1, 2, 4) were tuned. For GBT, the number of boosting stages (50, 100, 200), the learning rate (0.01, 0.1, 0.3), the maximum depth of each tree (3, 4, 5), the minimum number of samples per split (2, 5, 10), the minimum number of samples per leaf (1, 2, 4), and the fraction of samples used for each tree (0.8, 0.9, 1.0) were optimized. This systematic tuning ensured that all models were compared under well-calibrated configurations.

#### 4.2. Evaluation

A regression function  $g : \mathbb{R}^d \rightarrow \mathbb{R}$  aims to provide a sufficiently good approximation of the relationship between features and target values in the dataset. In the context of our study, given a feature vector  $x$  derived from a micro-CT image with apparent strength  $y$ , we want the function's approximation  $\hat{y} = g(x)$  to the bone strength to be near to the ground truth bone apparent strength  $y$ . To assess how well  $g$  performs, we need a quantitative measure of the prediction error.

The *root mean square error* (RMSE) measures the standard deviation of the residuals (prediction errors) and indicates the model's prediction accuracy. For  $n$  observations, it is defined as

$$\text{RMSE} = \sqrt{\frac{1}{n} \sum_{i=1}^n (y_i - \hat{y}_i)^2},$$

where  $y_i$  and  $\hat{y}_i$  denote the observed and predicted values for observation  $i$ , respectively.

The RMSE quantifies the average size of prediction errors in the same units as the target variable, with lower values indicating better accuracy. Apparent strength values in this study range from roughly 2.7 to 11.9 MPa. While the median strengths of NF and OA groups are very similar (9.0 versus 8.9 MPa), the FX group (4.7 MPa) differs from both NF and OA by at least 4.2 MPa. An RMSE well below this threshold indicates that the model captures meaningful biological variation, whereas an RMSE approaching the overall range suggests poor predictive performance. Medians were used to summarize group strengths because small sample sizes in some groups make mean estimates less reliable.

The *coefficient of determination*  $R^2$  assesses the proportion of variance in the target variable explained by the model:

$$R^2 = 1 - \frac{\sum_{i=1}^n (y_i - \hat{y}_i)^2}{\sum_{i=1}^n (y_i - \bar{y})^2},$$

where  $\bar{y}$  is the mean of the observed values. An  $R^2$  of 0 implies that the model performs no better than simply predicting the mean, while a negative  $R^2$  indicates performance worse than this naive baseline. A score of 1 represents a perfect fit, with the model explaining all variability in the target data.

In this study, we do not report the adjusted  $R^2$  because the dataset is small and the number of features greatly exceeds the number of observations. Under these conditions, adjusted  $R^2$  becomes unreliable and misleading.

Additionally, feature importance was assessed for the RF and GBT models to understand the relative contribution of each input feature to model predictions. Importance

for both tree-based models (Louppe *et al.*, 2013) was computed based on the mean decrease in impurity across all trees, which reflects how much each feature reduces prediction error when used for splits. Reporting these importance measures provides insight into which features are most predictive of apparent strength, facilitating interpretation and guiding future feature selection.

#### 4.3. Apparent Strength Prediction

We describe the performance of the each type of image-derived features highlighting how each feature type contributes to predictive performance.

##### 4.3.1. Bone Morphometry:

We begin the analysis by examining the performance of models trained on standard bone morphometric characteristics extracted from images binarized using local Otsu thresholding with window sizes of 3, 7, and 11. Table 1 summarizes the evaluation metrics of the best-performing models for each window size. Training using RF achieved the highest performance across all window sizes. Although a window size of 3 produced the lowest mean RMSE and highest mean  $R^2$ , its high variability indicates less stable predictions. In contrast, a window size of 7 yielded comparable mean accuracy but with substantially lower variability, suggesting stronger generalization. Increasing the window size further to 11 degraded performance, likely due to oversmoothing of morphological details during binarization. These findings highlight the sensitivity of BoneJ-derived features to the scale of local thresholding and suggest that a moderate window size best preserves structural information relevant for apparent strength prediction.

Table 1: Performance of best-performing models trained on standard bone morphometric descriptors, evaluated across different local Otsu thresholding window sizes.

Model	Window Size	RMSE		$R^2$	
		Mean	$\sigma^2$	Mean	$\sigma^2$
RF	3	1.8016	0.4473	0.3476	0.228
RF	7	1.8309	0.1862	0.3434	0.0837
RF	11	1.9450	0.1718	0.2508	0.127

Next, we assess the impact of including age as a predictor variable after applying top feature selection. In both processes, we utilize the images binarized with a window size of 7. Evaluation metrics for the best-performing models in both processes are presented in Table 2.

Incorporating patient age into the feature set yielded modest but consistent improvements. The mean RMSE decreased from 1.83 to 1.80, and the mean  $R^2$  increased from 0.34 to 0.37, with similar variability across folds.

Feature importance analysis identified trabecular thickness and spacing statistics as the most influential predictors, with the mean and standard deviation of trabecular thickness scoring 0.498 and 0.219 in normalized importance, respectively. Other features (including degree of anisotropy, maximum trabecular thickness, maximum trabecular spacing, and bone volume) contributed minimally.

Model training after removing the minimally important features slightly improved mean performance, though fold-level variability persisted, reflecting sensitivity to training-validation splits. Overall, these findings confirm that both feature selection and inclusion of demographic information can yield incremental performance gains without compromising stability, while trabecular thickness remains the dominant determinant of apparent strength estimation.

Table 2: Performance of best-performing models using standard bone morphometric features after including age as a predictor and applying top feature selection.

Model	Features	RMSE		$R^2$	
		Mean	$\sigma^2$	Mean	$\sigma^2$
RF	BoneJ with Age	1.8026	0.1891	0.3657	0.064
RF	BoneJ (Top 10)	1.7785	0.2144	0.3788	0.1054

To further lessen the computational load, the minimally important features as described above were removed.

Next, we assess the use of the modified Otsu method for binarization. Table 3 presents the evaluation metrics of the best-performing models across various window size and contrast parameter settings. Using the modified Otsu method, RF models with a window size of 3 and low contrast of 0.025 performed poorly, suggesting that overly local thresholding introduces noise and fragments structural features. GBT with a window size of 7 and contrast of 0.025 achieved the best performance, demonstrating robustness to feature variability induced by preprocessing. Similar to the standard Otsu method, increasing the window size worsened model performance, while higher contrast values also degraded accuracy.

Table 3: Performance of best-performing models trained on a subset of the standard bone morphometric descriptors, evaluated across different local modified Otsu window sizes and contrast parameters.

Model	Window Size	Contrast	RMSE		$R^2$	
			Mean	$\sigma^2$	Mean	$\sigma^2$
RF	3	0.025	2.5709	0.4615	-0.3473	0.5307
GBT	7	0.025	1.7135	0.2744	0.4175	0.1507
RF	9	0.025	1.9052	0.1919	0.2817	0.1413
GBT	9	0.05	2.0454	0.58	0.1523	0.3521

Finally, the same assessment was conducted using the local 2D Otsu binarization method. Table 4 summarizes the evaluation metrics for the best-performing models. The results indicate that an intensity window size of 7 combined with a mean window size of 3 achieves nearly the same performance as the previously tested thresholding methods. Increasing the mean window size beyond the intensity window size leads to a degradation in model performance. Moreover, configurations where the mean and intensity window sizes are close in value perform worse than those with a larger difference between the two. Overall, these findings suggest that 1D approaches can outperform this 2D method, even without incorporating the additional information used in the latter.

Table 4: Performance of best-performing models trained on a subset of the standard bone morphometric descriptors, evaluated across different local 2D Otsu window sizes.

Model	Intensity-Mean Window Sizes	RMSE		$R^2$	
		Mean	$\sigma^2$	Mean	$\sigma^2$
RF	(3, 3)	1.9328	0.3061	0.2562	0.2041
RF	(3, 5)	2.2135	0.2268	0.0302	0.1947
RF	(5, 5)	2.0141	0.2159	0.207	0.0948
RF	(7, 3)	1.7947	0.2022	0.3689	0.0927
RF	(7, 5)	1.9294	0.3067	0.2705	0.1551

Overall, these results emphasize the importance of preprocessing scale, feature relevance, and demographic context in achieving robust, biologically meaningful predictions of apparent bone strength.

#### 4.3.2. Persistent Homology:

Moving to persistent homology, we begin the analysis by examining persistence images (PIs) generated from the micro-CT data with grid resolution of  $50 \times 50$  and a variance of 1. As shown in Table 5, PIs outperformed bone morphometric features derived from 1D Otsu binarization but not those from 2D Otsu. In particular, 0-dimensional (0D) PIs provided the most informative representations. In contrast, higher-dimensional features were less predictive, and combining features from all dimensions did not enhance performance. These results suggest that topological features in micro-CT images contribute minimally to apparent strength prediction.

Table 5: Performance of best-performing models trained on persistence images obtained from the micro-CT images.

Model	Dimension	RMSE		$R^2$	
		Mean	$\sigma^2$	Mean	$\sigma^2$
GBT	0	1.6756	0.2596	0.4448	0.133
RF	1	1.905	0.3048	0.2891	0.1589
RF	2	2.0202	0.2663	0.1967	0.1605
GBT	0, 1, 2	1.7918	0.3881	0.3593	0.2366

Now, we assess the performance of persistence images generated from the signed distance transform of the micro-CT images. For brevity, we refer to these features as  $k$ -dimensional ( $k$ D) signed distance persistence images. As described in Definition 3.3.1, the SDT depends on the isotropic spacing of the images. For this initial analysis, we set the voxel spacing to 1 in all dimensions and later evaluate how performance changes when incorporating the actual voxel spacing of the micro-CT data.

Table 6: Performance of best-performing models trained on persistence images obtained from the signed distance transform of the micro-CT images.

Model	Dimension	RMSE		$R^2$	
		Mean	$\sigma^2$	Mean	$\sigma^2$
RF	0	1.9888	0.1883	0.1983	0.2364
GBT	1	1.767	0.252	0.3828	0.1358
GBT	2	1.1871	0.3262	0.7165	0.1151
RF	0, 1, 2	1.5549	0.2614	0.526	0.1042

For the following signed distance PIs, the binarization method used is the local Otsu with window size of 7. Moreover, the grid resolution is  $50 \times 50$  and the variance of the Gaussian kernel is 1. The evaluation metrics for the 2D signed distance PIs are presented in Table 6. Notably, using signed distance PIs as feature sets yielded the best performance observed so far. Specifically, the 2D signed distance PIs were highly predictive. Combination of the features from all dimensions offered no additional benefit.

Aside from isotropic spacing, another factor that may influence model performance is the binarization method used to generate the signed distance transform. Here, we investigate the effect of using local Otsu binarization with varying window sizes. As shown in Table 7, a window size of 9 yielded the best average performance and the most consistent predictive ranges, whereas both smaller and larger windows degraded performance. These results suggest that a moderate neighborhood size effectively balances noise reduction with the preservation of relevant topological information.

Table 7: Performance of best-performing models trained on 2D signed distance persistence images, evaluated across different local Otsu window sizes.

Model	Window Size	RMSE		$R^2$	
		Mean	$\sigma^2$	Mean	$\sigma^2$
GBT	5	1.2645	0.293	0.6843	0.103
GBT	9	1.0592	0.3819	0.7696	0.1351
GBT	11	1.2194	0.3915	0.6872	0.1639

The generation of persistence images depends on the chosen grid resolution and Gaussian kernel variance. We next explore the effect of varying these parameters. The best-performing models are summarized in Table 8. Optimal performance was achieved with a variance of 1 and a resolution of  $25 \times 25$ . Deviating from this bandwidth or increasing the resolution did not consistently improve performance and often increased variability, indicating a trade-off between feature detail and stability.

Table 8: Performance of best-performing models trained on 2D signed distance persistence images, evaluated across varying variances and resolutions.

Model	Variance	Resolution	RMSE		$R^2$	
			Mean	$\sigma^2$	Mean	$\sigma^2$
GBT	0.5	$50 \times 50$	1.59	0.232	0.5077	0.0798
GBT	1	$15 \times 15$	1.0429	0.2798	0.7817	0.0881
GBT	1	$25 \times 25$	0.9678	0.2865	0.8114	0.0855
GBT	1	$50 \times 50$	1.0592	0.3819	0.7696	0.1351
GBT	1.25	$25 \times 25$	1.1828	0.234	0.7217	0.0846
GBT	1.5	$50 \times 50$	1.3376	0.1748	0.6506	0.0542

For the final set of simulations, several methodological variations were introduced to assess their impact on model performance. The tested configurations and parameters are summarized in Table 9, with image resolution fixed at  $25 \times 25$ . Changing the binarization method from Otsu to the modified Otsu substantially decreased predictive performance. Similarly, reversing the sign in the Euclidean signed distance transform (as described in Definition 3.3.1) also degraded performance, although the results remained superior to those of all BoneJ-trained models. This shows that model performance is sensitive to the choice of binarization, highlighting the need for segmentation that faithfully preserves topological structure.

The placement of the negative sign highlights that 0D signed distance PIs are highly informative. In this context, the main morphological variation arises from the formation and merging of bone regions rather than from the spacing of voids, providing a complementary perspective on the microarchitecture previously captured through void-based 2D features. In some cases, this approach may also be more computationally efficient, as it requires only 0-dimensional features rather than computing higher-dimensional topological features.

Finally, when the actual isotropic voxel spacing from each micro-CT image was incorporated, model performance declined further, becoming comparable to that of the BoneJ-trained models. This outcome suggests that explicitly encoding voxel spacing may introduce scale-related distortions that obscure intrinsic topological relationships. Conversely, methods that abstract away from voxel-dependent metrics may offer better generalizability across imaging systems and resolutions, an important consideration as higher-resolution imaging modalities continue to emerge. Additional experiments varying grid resolution and Gaussian kernel variance may be necessary to better understand this effect.

Topological features, particularly those derived from 2D signed distance persistence images, proved highly predictive of bone strength, significantly outperforming standard morphometric approaches. The dominance performance underscores a critical insight: the primary morphological signal originates from the distribution of voids within the bone structure.

As detailed in subsection [Section 3.3](#), these 2D features are organized by their position in the birth–death plane, which allows for a distinction between true microstructural signal and potential noise. Features in the first quadrant capture the true microstructural signal by characterizing interspace sizes and directly quantify void spacing (and, complementarily, trabecular thickness). Features in the second quadrant reflect noise, specifically small bone inclusions within empty regions. These inclusions are likely spurious voids generated by thresholding errors or imaging artifacts and do not represent genuine trabecular microstructure.

Table 9: Performance of models trained on 2D signed distance persistence images obtained by incorporating different methods.

Model	Method	Variance	Dimension	RMSE		$R^2$	
				Mean	$\sigma^2$	Mean	$\sigma^2$
RF	Modified Otsu	1	2	1.9024	0.4461	0.222	0.3992
GBT	Otsu (Reverse)	1	0	1.2813	0.2382	0.6765	0.0829
GBT	Otsu (Spacing)	1	2	1.5689	0.4448	0.4887	0.2279
GBT	Otsu (Spacing)	$5.4 \times 10^{-5}$	2	1.5402	0.3491	0.5285	0.1531

While these “fictitious” voids might initially seem like irrelevant noise, their detection is highly significant. It immediately highlights the sensitivity of the topological methods while also pointing to a limitation of conventional imaging techniques. Ultimately, this sensitivity suggests that topological approaches have a dual benefit. They not only predict mechanical properties effectively but also hold potential to guide improvements in imaging and segmentation strategies.

The finetuned hyperparameters for the best-performing model, which is the GBT trained on the signed distance persistence images with a resolution of  $25 \times 25$  and variance 1, derived from the micro-CT images binarized using a local Otsu method with a window size of 9, are as follows: a learning rate of 0.01, a maximum tree depth of 3, a minimum of 2 samples per leaf, a minimum of 10 samples required to split a node, a fraction of 1 of samples used for each tree, and 200 boosting stages.

## 5. CONCLUSION AND FUTURE DIRECTIONS

Persistent homology reveals that topological descriptors can outperform traditional morphometric measures in predicting bone strength, highlighting the biomechanical importance of internal voids often overlooked in conventional analyses. Integrating these topological features with standard metrics enhances predictive accuracy while capturing subtle microarchitectural details that conventional approaches miss.

This study establishes a new paradigm for bone image analysis, prioritizing topological complexity over density or geometric measures, and lays the foundation for non-invasive computational biomarkers. These findings open the door to advanced CT-based assessments that could complement or potentially reduce reliance on bone biopsies, with implications for both research and clinical applications.

Future mathematical investigations may explore neural network–based approaches that incorporate topological information, as well as further analyses of the signed distance transform, including medial axis representations, to better understand the relationship between bone microarchitecture and mechanical properties. Expanding

the dataset to include a broader range of bone conditions and validating models on independent cohorts will be crucial for assessing generalizability.

Additionally, future work should evaluate the topological markers against fracture outcomes and examine their integration into diagnostic workflows. This approach shows promise for applications in chronic kidney disease-associated osteoporosis (Hsu *et al.*, 2020), where bone quality rather than density is a key determinant of fragility. Topological biomarkers could also serve as sensitive endpoints in drug efficacy trials, detecting microarchitectural responses to treatment, and support longitudinal monitoring of bone health in aging or disease progression (Chen, 2024).

## 6. ACKNOWLEDGMENTS

We gratefully acknowledge the support from the Dioscuri Program as well as hosting by the Institute of Mathematics Polish Academy of Sciences.

## REFERENCES

- Adams, H., Emerson, T., Kirby, M., Neville, R., Peterson, C., Shipman, P., Chepushtanova, S., Hanson, E., Motta, F., & Ziegelmeier, L. (2017). Persistence Images: A Stable Vector Representation of Persistent Homology. *Journal of Machine Learning Research*, 18(8), 1–35. <http://jmlr.org/papers/v18/16-337.html>
- Breiman, L. (2001). Random Forests. *Machine Learning*, 45(1), 5–32. <https://doi.org/10.1023/a:1010933404324>
- Chen, D. (2024). Biomarkers navigate drug development: Pharmacology, effectiveness and safety. *Medicine in Drug Discovery*, 21, 100174. <https://doi.org/10.1016/j.medidd.2023.100174>
- Cohen-Steiner, D., Edelsbrunner, H., & Harer, J. (2006). Stability of Persistence Diagrams. *Discrete & Computational Geometry*, 37(1), 103–120. <https://doi.org/10.1007/s00454-006-1276-5>
- Dahl, V. A., & Dahl, A. B. (2023). Fast Local Thickness. *2023 IEEE/CVF Conference on Computer Vision and Pattern Recognition Workshops (CVPRW)*, 4336–4344. <https://doi.org/10.1109/cvprw59228.2023.00456>
- Domander, R., Felder, A., & Doube, M. (2021). BoneJ2 - refactoring established research software [version 2; peer review: 3 approved]. *Wellcome Open Research*, 6(37). <https://doi.org/10.12688/wellcomeopenres.16619.2>
- Engelkes, K. (2021). Accuracy of bone segmentation and surface generation strategies analyzed by using synthetic CT volumes. *Journal of Anatomy*, 238(6), 1456–1471. <https://doi.org/10.1111/joa.13383>
- Fanuscu, M. I., & Chang, T.-L. (2004). Three-dimensional morphometric analysis of human cadaver bone: microstructural data from maxilla and mandible. *Clinical Oral Implants Research*, 15(2), 213–218. <https://doi.org/10.1111/j.1600-0501.2004.00969.x>
- Friedman, J. H. (2001). Greedy function approximation: A gradient boosting machine. *The Annals of Statistics*, 29(5). <https://doi.org/10.1214/aos/1013203451>
- Gazzotti, S., Aparisi Gómez, M. P., Schileo, E., Taddei, F., Sangiorgi, L., Fusaro, M., Miceli, M., Guglielmi, G., & Bazzocchi, A. (2023). High-resolution peripheral quantitative computed tomography: research or clinical practice?. *The British Journal of Radiology*, 96(1150). <https://doi.org/10.1259/bjr.20221016>
- Hsu, C.-Y., Chen, L.-R., & Chen, K.-H. (2020). Osteoporosis in Patients with Chronic Kidney Diseases: A Systemic Review. *International Journal of Molecular Sciences*, 21(18), 6846. <https://doi.org/10.3390/ijms21186846>
- Issever, A. S., Link, T. M., Kentenich, M., Rogalla, P., Burghardt, A. J., Kazakia, G. J., Majumdar, S., & Diederichs, G. (2009). Assessment of trabecular bone structure using MDCT: comparison of 64- and 320-slice CT using HR-pQCT as the reference standard. *European Radiology*, 20(2), 458–468. <https://doi.org/10.1007/s00330-009-1571-7>
- Jin, A. (2016, May). *The effect of bisphosphonates on bone microstructure and strength*. <https://doi.org/10.25560/49791>
- Kaczynski, T., Mischaikow, K., & Mrozek, M. (2004). *Computational Homology*. Springer New York. <https://doi.org/10.1007/b97315>
- Larrue, A., Rattner, A., Peter, Z.-A., Olivier, C., Laroche, N., Vico, L., & Peyrin, F. (2011). Synchrotron Radiation Micro-CT at the Micrometer Scale for the Analysis of the Three-Dimensional Morphology of Microcracks in Human Trabecular Bone. *Plos ONE*, 6(7), e21297. <https://doi.org/10.1371/journal.pone.0021297>
- Loupe, G., Wehenkel, L., Sutura, A., & Geurts, P. (2013). Understanding variable importances in forests of randomized trees. In C. Burges, L. Bottou, M. Welling, Z. Ghahramani, & K. Weinberger (Eds.), *Advances in*

*Neural Information Processing Systems: Vol. 26. Advances in Neural Information Processing Systems*. [https://proceedings.neurips.cc/paper\\_files/paper/2013/file/e3796ae838835da0b6f6ea37bcf8bcb7-Paper.pdf](https://proceedings.neurips.cc/paper_files/paper/2013/file/e3796ae838835da0b6f6ea37bcf8bcb7-Paper.pdf)

- Morgan, S. L., & Prater, G. L. (2017). Quality in dual-energy X-ray absorptiometry scans. *Bone*, *104*, 13–28.
- Park, S. A., Sipka, T., Krivá, Z., Lutfalla, G., Nguyen-Chi, M., & Mikula, K. (2023). Segmentation-based tracking of macrophages in 2D+time microscopy movies inside a living animal. *Computers in Biology and Medicine*, *153*, 106499. <https://doi.org/10.1016/j.combiomed.2022.106499>
- Pritchard, Y., Sharma, A., Clarkin, C., Ogden, H., Mahajan, S., & Sánchez-García, R. J. (2023). Persistent homology analysis distinguishes pathological bone microstructure in non-linear microscopy images. *Scientific Reports*, *13*(1), 2522. <https://doi.org/10.1038/s41598-023-28985-3>
- Schroeder, A. B., Dobson, E. T. A., Rueden, C. T., Tomancak, P., Jug, F., & Eliceiri, K. W. (2021). The ImageJ ecosystem: Open-source software for image visualization, processing, and analysis. *Protein Science*, *30*(1), 234–249. <https://doi.org/10.1002/pro.3993>
- Smola, A. J., & Schölkopf, B. (2004). A tutorial on support vector regression. *Statistics and Computing*, *14*(3), 199–222. <https://doi.org/10.1023/b:stco.0000035301.49549.88>
- Song, A., Yim, K. M., & Monod, A. (2025). Generalized Morse theory of distance functions to surfaces for persistent homology. *Advances in Applied Mathematics*, *166*, 102857. <https://doi.org/10.1016/j.aam.2025.102857>
- U.S. Food and Drug Administration. (2024, ). *BoneJ Headless: An Automated Python Tool for Bone Microstructure Analysis (RST24AI03.01)*. <https://cdrh-rst.fda.gov/bonej-headless-automated-python-tool-bone-microstructure-analysis>
- Walt, S. van der, Schönberger, J. L., Nunez-Iglesias, J., Boulogne, F., Warner, J. D., Yager, N., Gouillart, E., & Yu, T. (2014). scikit-image: image processing in Python. *PeerJ*, *2*, e453. <https://doi.org/10.7717/peerj.453>
- Zhang, J., & Hu, J. (2008). Image Segmentation Based on 2D Otsu Method with Histogram Analysis. *2008 International Conference on Computer Science and Software Engineering*, 105–108. <https://doi.org/10.1109/csse.2008.206>